ACSNANO

www.acsnano.org

ARTICLE

High-Voltage Long-Cycling All-Solid-State Lithium Batteries with High-Valent-Element-Doped Halide Electrolytes

Yu Ye,[#] Jiazhong Geng,[#] Daxian Zuo,[#] Kangdi Niu, Diancheng Chen, Junhao Lin, Xihan Chen,* Haw Jiunn Woo,* Yizhou Zhu,* and Jiayu Wan*

Cite This: *ACS Nano* 2024, 18, 18368−18378

Read Online

ACCESS | Metrics & More | Article Recommendations | Supporting Information

ABSTRACT: All-solid-state batteries (ASSBs) have garnered considerable attention as promising candidates for next-generation energy storage systems due to their potentially simultaneously enhanced safety capacities and improved energy densities. However, the solid future still calls for materials with high ionic conductivity, electrochemical stability, and favorable interfacial compatibility. In this study, we present a series of halide solid-state electrolytes (SSEs) utilizing a doping strategy with highly valent elements, demonstrating an outstanding combination of enhanced ionic conductivity and oxidation stability. Among these, $Li_{2.6}In_{0.8}Ta_{0.2}Cl_6$ emerges as the standout performer, displaying a superionic conductivity of up to 4.47 mS cm^{-1} at 30 °C, along with a low activation energy barrier of 0.321 eV for Li^+ migration. Additionally, it showcases an extensive oxidation onset of up to 5.13 V (vs Li^+/Li), enabling high-voltage ASSBs with promising cycling performance. Particularly noteworthy are the ASSBs employing $LiCoO_2$ cathode materials, which exhibit an extended cyclability of over 1400 cycles, with 70% capacity retention under 4.6 V (vs Li^+/Li), and a capacity of up to 135 mA h g^{-1} at a 4 C rate, with the loading of active materials at 7.52 mg cm^{-2}. This study demonstrates a feasible approach to designing desirable SSEs for energy-dense, highly stable ASSBs.

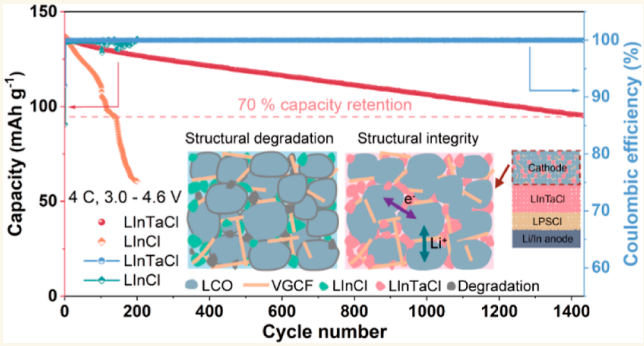

KEYWORDS: *all-solid-state batteries, halide solid-state electrolytes, high-valent doping, high voltage, ionic conductivity*

INTRODUCTION

The European Union, the United States, and China have been advocating for reducing greenhouse gas emissions, aiming to achieve net-zero targets by the 2050s through initiatives such as industrial decarbonization and the development of smart cities, aligning with Sustainable Development Goal 7. Rechargeable batteries play a pivotal role in reducing the carbon footprint when utilized to power electric vehicles and grid-scale storage, particularly lithium-ion batteries (LIBs).[1−3] However, using flammable liquid electrolytes in conventional battery systems has given rise to safety concerns, leading to explosions in severe cases. Beyond LIBs, all-solid-state batteries (ASSBs) have emerged as promising candidates for the energy storage devices of the next generation.[4,5] ASSBs hold the potential to achieve elevated energy densities while simultaneously enhancing safety.[6] Central to the functioning of ASSBs, solid-state electrolytes (SSEs) play a crucial role as an essential component. They are meticulously selected for their superionic conductivity and high voltage stability, thus underpinning the overall enhancement of the batteries.[7,8]

Over the past decades, various materials have been developed in SSE research, with garnet-type oxide and sulfide SSEs standing out as the most extensively studied materials.[9−12] Garnet-type oxide-based SSEs often exhibited good chemical stability with Li metal.[13] However, the challenges of high synthesis temperatures and inherent brittleness in ceramic oxides pose significant hurdles in processing and interface contact, impeding their broad application in ASSBs.[14] Sulfide SSEs have garnered increasing attention due to their high ionic conductivity (up to 32 mS cm^{-1}) and soft nature.[15−18] These

Received: February 26, 2024
Revised: June 17, 2024
Accepted: June 18, 2024
Published: July 6, 2024

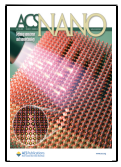

Downloaded via WESTLAKE UNIV on November 18, 2024 at 02:09:31 (UTC).
See https://pubs.acs.org/sharingguidelines for options on how to legitimately share published articles.

ACS Publications © 2024 American Chemical Society

https://doi.org/10.1021/acsnano.4c02678
ACS Nano 2024, 18, 18368−18378

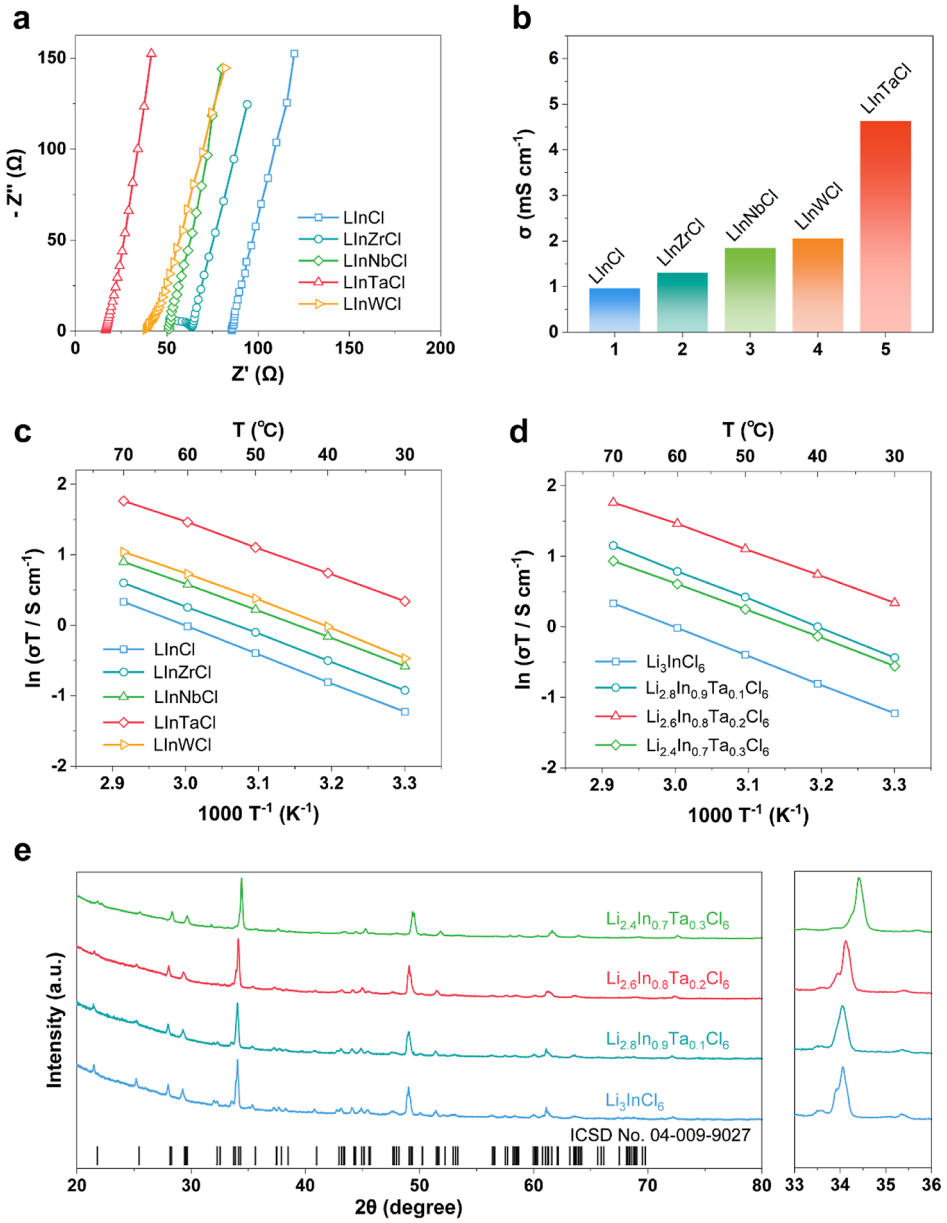

Figure 1. Ionic conductivity and XRD results of high-valent-element-substituted Li_3InCl_6SSEs: (a) Nyquist plots at 30 °C, (b) ionic conductivity comparison at 30 °C (details in Figures S3−S5 and summarized in Table S1),[22−29,32,33,41−43] and (c) Arrhenius plots of Li_3InCl_6, $Li_{2.8}In_{0.8}Zr_{0.2}Cl_6$, $Li_{2.6}In_{0.8}Nb_{0.2}Cl_6$, $Li_{2.6}In_{0.8}Ta_{0.2}Cl_6$, and $Li_{2.4}In_{0.8}W_{0.2}Cl_6$ (from 30 to 70 °C). (d) Arrhenius plots and (e) XRD patterns (Cu Kα radiation) of $Li_{3-2x}In_{1-x}Ta_xCl_6$.

properties confer notable benefits by mitigating solid−solid contact resistance and enhancing the ionic transport within ASSBs. However, the narrow electrochemical stability windows of sulfide materials bound their potential use with high-voltage cathode materials that typically operate above 4.3 V (vs Li/Li^+). Consequently, a protective coating becomes necessary to insulate side reactions between the cathode materials and the electrolytes. Such reactions can lead to the degradation of the cathode−electrolyte interface and deteriorate battery performance.[19,20] Despite recent strides in SSE investigation, significant challenges hinder their practical implementation. There has been a renewed emphasis on halides as promising candidates to address the demand for SSEs with superionic conductivity, high oxidation stability, and favorable interfacial compatibility.[21]

In 2018, Asano et al. achieved a breakthrough by enhancing the room-temperature (RT) ionic conductivity of halide SSEs to the level of 1 mS cm^{-1}.[22] This was accomplished by synthesizing Li_3YCl_6 and Li_3YBr_6 through a combination of high-energy ball milling and high-temperature sintering. Subsequently, a series of halide SSEs with RT ionic conductivity of 1 mS cm^{-1} has been developed, including Li_3InCl_6,[23] Li_xScCl_{3+x},[24] $Li_2In_xSc_{0.666-x}Cl_4$,[25] Li_2ZrCl_6,[26] $LiTaCl_6$,[27] $Li_{1.75}ZrCl_{4.75}O_{0.5}$,[28] and LiTa(Nb)$OCl_4$.[29] To achieve the high ionic conductivities necessary for practical battery cycling, research efforts in ternary metal halides have been focused on employing chemical substitutions.[30] A common practice involves aliovalent substitutions, such as incorporating Zr^{4+} or Hf^{4+} for the trivalent elements, driving enhanced ionic conductivities across various Li_3MCl_6 structures owing to the formation of mobile ion vacancies.[31,32] Recently, Yin et al.

https://doi.org/10.1021/acsnano.4c02678
ACS Nano 2024, 18, 18368−18378

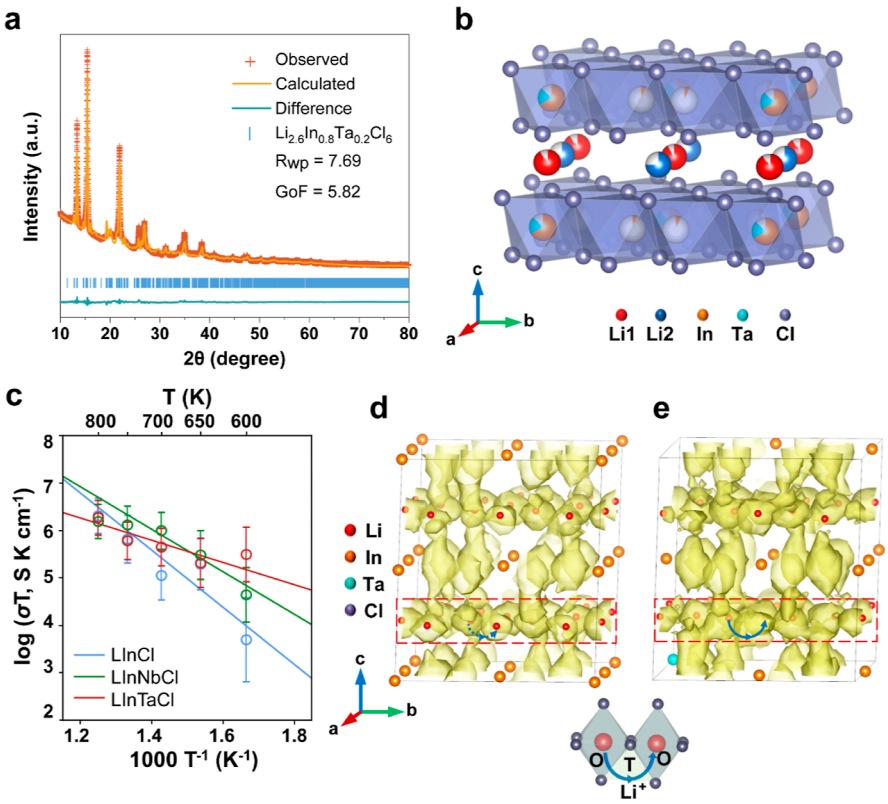

Figure 2. Structure and AIMD simulations of $Li_{2.6}In_{0.8}Ta_{0.2}Cl_6$. (a) XRD pattern from high-resolution synchrotron radiation and corresponding Rietveld refinement profiles; R_{wp} and GoF are the weighted profile *R*-factor and goodness-of-fit, respectively; the crystallographic data in CIF format is shown in Supporting Information 2. (b) Structure from refinement. (c) Arrhenius plots of Li^+ conductivity for LInCl and LInMCl from AIMD simulations (detailed in Table S4). The probability density of Li^+ in (d) LInCl and (e) LInTaCl, marked with yellow isosurfaces from AIMD simulation at 800 K with metal atoms shown in the lattices (O: octahedral; T: tetrahedron).

published a study on lanthanide metal chlorides, which demonstrated exceptional interfacial compatibility with lithium metal electrodes and showcased a superionic conductivity surpassing 3.02 mS cm^{-1} at 30 °C.[33] Additionally, these researchers established that halide SSEs exhibited favorable compatibility with 4 V-class $LiCoO_2$ (LCO) and ternary lithium cathodes, resulting in advantageous capacities and high initial Coulombic efficiencies for ASSBs.[34] Despite research attention keenly directed toward elucidating the intricacies of the oxidative stability inherent in metal chloride SSEs, the pursuit of devising SSBs capable of seamless operation beyond the 4.5 V threshold, coupled with fast-charging performance, still leaves room for further improvement.

Herein, we present an approach to the design of halide SSEs by introducing highly valent elements into the Li_3InCl_6 model system. Doping with high-valent cations in Li_3InCl_6 reduces the number of lithium ions to maintain charge balance in the lattice, creating additional vacant sites that can potentially improve ionic conductivity, as observed in other solid electrolytes such as LLZO.[35,36] This strategy, proposed in the theoretical work of Liu et al.,[37] suggests that tuning lithium stoichiometry to achieve an optimal value of 40−60% of available sites is a key principle for designing halide Li-ion conductors. Taking inspiration from this concept, we investigated a family of high-valent halide SSEs denoted as LInMCl SSEs (M = Zr, Nb, Ta, or W). Among these, $Li_{2.6}In_{0.8}Ta_{0.2}Cl_6$ demonstrated superionic conductivity with a low activation energy (reaching up to 4.47 mS cm^{-1} at 30 °C, 0.321 eV) and a high practical oxidation onset (5.13 V, vs Li/Li^+). We further demonstrated the superior electrochemical oxidation and cycling stability of our SSE in the form of ASSBs with LCO or $LiNi_{0.8}Co_{0.1}Mn_{0.1}O_2$ (NCM811) cathodes. These ASSBs exhibited excellent long-term cycling stability at RT, maintaining 70% capacity retention over more than 950 cycles with commercial LCO or NCM811 cathodes. Moreover, the battery cycled under a high voltage at 4.6 V with an LCO cathode displayed superior long-term cycling performance, retaining over 70% of its capacity for 1400 cycles at a 4 C rate with an active material loading of 7.52 mg cm^{-2}. Our work provides a design strategy that achieves high-performance halide SSEs by introducing high-valent elements, broadening avenues for implementing energy-dense ASSBs.

RESULTS AND DISCUSSION

Structure and Ionic Conductivity Properties of High-Valent Halide SSEs. Our halide SSEs were prepared with LiCl, $InCl_3$, and high-valent metal chlorides ($ZrCl_4$, $NbCl_5$, $TaCl_5$, and WCl_6) using a mechanochemically ball-milling method, followed by a low-temperature annealing process (260 °C, 5 h).[38] Figure S1 shows the X-ray diffraction (XRD) patterns of $Li_{2.8}In_{0.8}Zr_{0.2}Cl_6$ (LInZrCl), $Li_{2.6}In_{0.8}Nb_{0.2}Cl_6$ (LInNbCl), $Li_{2.6}In_{0.8}Ta_{0.2}Cl_6$ (LInTaCl), $Li_{2.4}In_{0.8}W_{0.2}Cl_6$ (LInWCl), and Li_3InCl_6 (LInCl) samples, indexed in the same space group as the LInCl structure,[39] with no phase transition observed. To delve into the influence of high-valent elements on Li^+-ion conductivities and migration energy, we

https://doi.org/10.1021/acsnano.4c02678
ACS Nano 2024, 18, 18368−18378

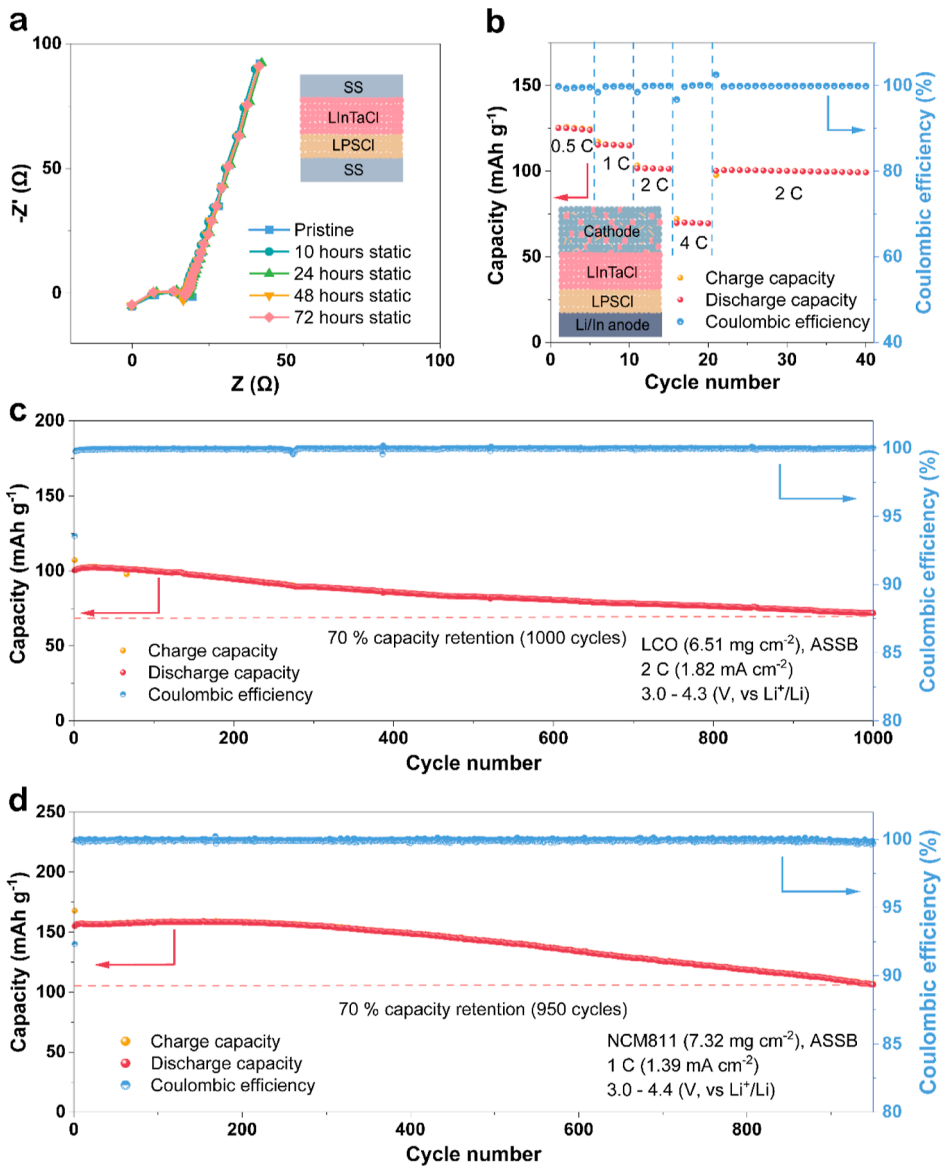

Figure 3. Electrochemical performance of ASSBs based on high-valent halide electrolytes. (a) EIS spectra of the SS//LPSCl//LiInTaCl//SS cells during a static period of 72 h. (b) Rate performance and Coulombic efficiency at 0.5, 1, 2, and 4 C for the LCO//LInTaCl//LPSCl//Li−In ASSB. Long-term cycling performance (c) at a 2 C rate for the LCO//LInTaCl//LPSCl//Li−In ASSB and (d) at a 1 C rate for the NCM811//LInTaCl//LPSCl//Li−In ASSB.

performed temperature-dependent electrochemical impedance spectroscopy (EIS). LInTaCl exhibited a superionic conductivity of 4.47 mS cm^{-1} (30 °C) along with a low activation energy of 0.321 eV. In contrast, the pristine LInCl sample showed a considerably lower Li^+ conductivity of 0.97 mS cm^{-1} and a higher activation energy of 0.401 eV (Figure 1a−c). Moreover, we explored the high-valent effects of $Li_{3-2x}In_{1-x}Ta_xCl_6$ ($0 < x \leq 0.3$). The ionic conductivity and activation energy are depicted in Figures 1d and S2; all the $Li_{3-2x}In_{1-x}Ta_xCl_6$ samples exhibited high ionic conductivity between 1.89 and 4.47 mS cm^{-1} (when $x = 0.2$) with a low activation energy from 0.32 to 0.36 eV. As shown in the XRD patterns in Figure 1e, the incorporation of Ta resulted in slight angle shifts to the right in the diffraction peak, owing to the reduction of ion radius size ($r_{Ta}{}^{5+} = 0.64$ Å, $r_{In}{}^{5+} = 0.8$ Å) and the decrease in lithium content within the unit cells, suggesting a decrease of crystalline interplanar spacing. Energy-dispersive spectroscopy (EDS) results shown in Figure S6 from double Cs-corrected transmission electron microscopy (TEM) reveal a highly homogeneous dispersion of 3 elements, including In, Ta, and Cl, further evidenced by the formation of a LInTaCl halide solid electrolyte.[40]

To better understand the structural influence of Ta^{5+} doping based on Li_3InCl_6, XRD Rietveld refinement against the synchrotron radiation of $Li_{2.6}In_{0.8}Ta_{0.2}Cl_6$ is displayed in Figure 2a (the crystallographic details are summarized in Table S2). The lattice parameters converged to $a = 6.35$ Å, $b = 10.9149$ Å, $c = 6.311$ Å and $\alpha = 90°$, $\beta = 108.844°$, $\gamma = 90°$, signifying a decreasing volume of the unit cell with the incorporation of Ta benefiting from the shrinkage in metal ionic radii. The structure of LInTaCl with the $C2/m$ space group contains two lithium octahedral positions Li1 and Li2 in the (002) lattice plane (Figure 2b).[31] To investigate the Li^+ diffusivity of LInCl and high-valent SSEs with structural parameters changed (Table S3), ab initio molecular dynamics (AIMD) simulations[44] were performed (Figures 2c and S9). The active

https://doi.org/10.1021/acsnano.4c02678
ACS Nano 2024, 18, 18368−18378

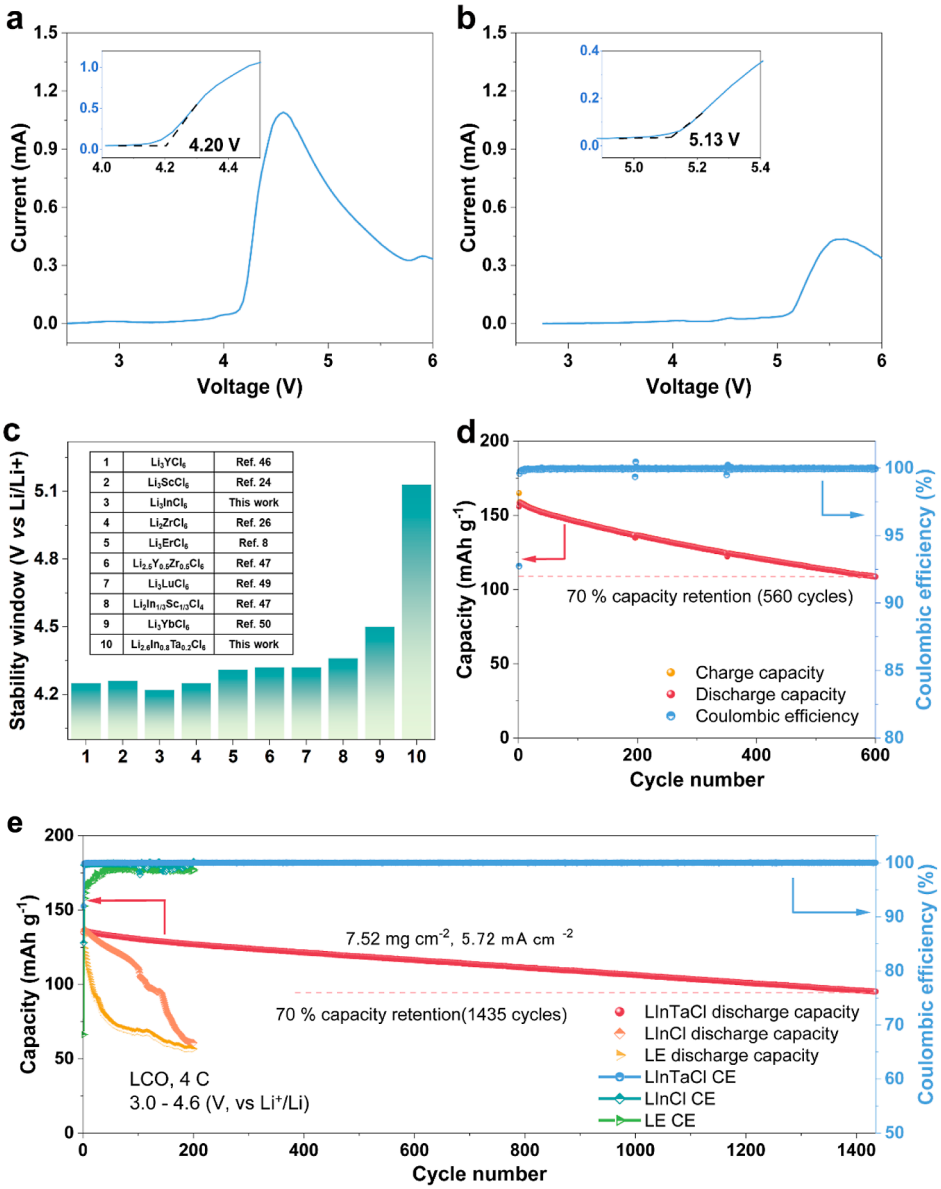

Figure 4. Electrochemical windows and high-voltage ASSB performance based on high-valent halide electrolytes. LSV curves for (a) LInCl-VGCF and (b) LInTaCl-VGCF composite from OCP to 6 (V, vs Li/Li$^+$). (c) Oxidation onset comparison with typical metal chloride solid electrolytes (detailed in Figure S17).[24,26,46−50] (d) Long-term cycling performance and CE at 2 C for a 4.6 V (vs Li/Li$^+$) LCO//LInTaCl////LPSCl//Li−In ASSB (the CV results of the ASSB are shown in Figure S18). (e) Cycling performance of high-voltage high-rate LCO batteries with LInTaCl, LInCl, and liquid electrolyte (1 mol $LiPF_6$ in EC/DEC/EMC = 1:1:1, cathode active material loading = 3 mg cm^{-2}).

ion hopping in doped systems can be proven from the lower activation energies of LInNbCl (0.18 eV) and LInTaCl (0.29 eV) compared with that of LInCl (0.44 eV). The extrapolated Li$^+$ conductivities of LInTaCl and LInNbCl from AIMD calculations are 21.27 and 1.87 mS cm^{-1} at 300 K, respectively. The extrapolated RT ionic conductivities of the M^{5+}-doped structures are significantly larger than that of LInCl (0.05 mS cm^{-1}). To understand the origin of enhanced Li$^+$ conductivity in the doped samples, probability densities of Li$^+$ from the AIMD simulation were calculated at 800 K (Figures 2d,e and S8). From the result, most of the Li$^+$ distribution is located at the octahedral sites, while tetrahedral interstitial sites play interlinked roles in the lithium-ion conducting paths, forming typical o−t−o diffusion paths in the *fcc* anion sublattice. Comparing the pristine to the doped LInCl, the probability density of Li$^+$ along the o−t−o paths within the *ab*-plane lithium networks increases, facilitating improved conductivity through continuously interconnected octahedral site hopping in doped LInCl lattices. Doping of high-valent metal ions introduces extra lithium vacancies in the LInCl lattice. These vacancies, occupying octahedral sites, are crucial for the low-energy-barrier transport of lithium ions. The increasing Li$^+$ migration found in high-valent SSEs is consistent with the designing principles demonstrated by Liu et al.,[37] which proposed that low Li content, low cation concentration, and sparse cation distribution increase Li$^+$ conduction in chlorides. The increase in the ratio of low-energy-barrier diffusion paths in the doped LInCl lattice benefits the percolation network of lithium ions and leads to high ionic conductivity.

ASSB Performance Based on High-Valent Halide Electrolytes. To evaluate the compatibility of LInTaCl with LPSCl, we conducted EIS experiments using SS//LPSCl//

https://doi.org/10.1021/acsnano.4c02678
ACS Nano 2024, 18, 18368−18378

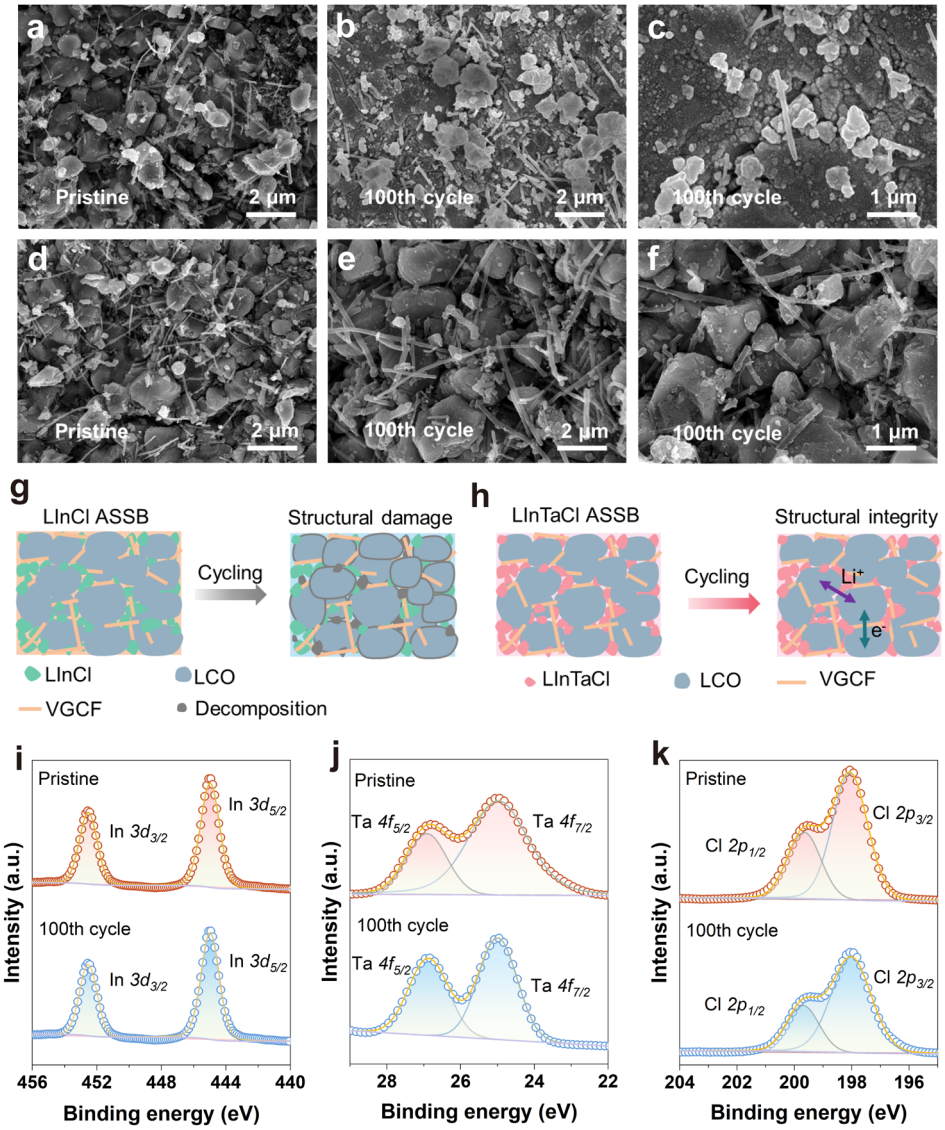

Figure 5. Morphology and XPS evolution of the cathode composite during the electrochemical process. (a−f) FESEM images of the electrode during cycling of (a−c) LInCl and (d−f) LInTaCl. (g, h) Schematic illustrations of (g) LInCl cathode active materials and (h) LInTaCl during cycling. (i−k) XPS analysis of In 3d, Ta 4f, and Cl 2p for LInTaCl during cycling.

LInTaCl//SS cells.[45] Figure 3a demonstrates that LInTaCl maintains good compatibility with LPSCl, evidenced by no significant increase in impedance. Additionally, X-ray photoelectron spectroscopy (XPS) analysis before and after a 72 h static test (Figure S10) confirms no changes in chemical valence states, substantiating the stability of LInTaCl when combined with LPSCl. To test the performance of the as-prepared LInTaCl SSE in full cells, we assembled ASSBs with a LCO cathode and Li−In anode, while LPSCl was used as an interlayer to prevent possible side decomposition of the halide electrolyte at the anode side. We tested the rate performances of the ASSB as shown in Figures 3a and S11 [cutoff voltage of 4.3 V (vs Li/Li$^+$) at 30 °C], and a notable rate capability was observed. The ASSB delivered specific capacities of 125 mA h g^{-1} at a rate of 0.5 C and 70 mA h g^{-1} at 4 C with a loading of 6.56 mg cm^{-2}. We further conducted long-term cycling at a 2 C rate and a current density of 1.82 mA cm^{-2}, in which the LCO//LInTaCl//LPSCl//Li−In ASSB exhibited an excellent cycling performance enabling an average Coulombic efficiency of 99.9% and maintained 70% capacity retention after 1000 extended cycles (Figures 3c and S12). Moreover, we assembled and tested the ASSB with an NCM811 cathode at a voltage of 4.4 V (vs Li/Li$^+$) and a 1 C rate (loading of 7.32 mg cm^{-2}), achieving a capacity retention of 70% after 950 extended cycles, as shown in Figures 3d and S13.

High-Voltage Electrochemical Performance of ASSBs. To understand the performance of the LInTaCl SSE at high voltage, linear cyclic voltammetry (LSV) was performed using halide electrolytes and a halide electrolyte/carbon vapor growth carbon fiber (VGCF) cathode. Figure 4a,b illustrates the cathodic scan curves of LInCl and LInTaCl, respectively, within a voltage range from open-circuit potential (OCP) to 6 V (vs Li/Li$^+$) with a scan rate of 0.5 mV s^{-1}. The oxidation onset of the LInCl control sample emerges around 4.22 V, and the peak oxidation current reaches 1.08 mA at 4.57 V, identifying the sharp oxidation behaviors in the first cycle, which agrees with other studies.[46] It was found that the stability of LInTaCl markedly exceeds that of LInCl, manifesting superior attributes concerning the oxidation onset (5.13 V, vs Li/Li$^+$) and the extent of the electrochemical

https://doi.org/10.1021/acsnano.4c02678
ACS Nano 2024, 18, 18368−18378

reaction. Figure 4c compares oxidation onset to typical metal chloride solid electrolytes from experimental measurement. Manifestly, the observed 5.13 V-oxidation threshold delineated in this study delineates LInTaCl as a preeminent high-voltage chloride-based solid electrolyte, thus accentuating its prominence in the field.[24,26,46−50] The outstanding electrochemical stability results from LSV indicate the possibility of utilizing a LInTaCl SSE for the performance for high-voltage ASSBs, which we increased the operation voltage with the LCO cathode to 4.6 V (vs Li/Li^+). The LCO ASSB cycled at a 2 C rate released an initial discharge capacity of 156 mA h g^{-1} and obtained a capacity of over 108 mA h g^{-1} (70% capacity retention) after 560 charge−discharge cycles (Figures 4d and S14). Moreover, as shown in Figures 4e and S15, the same type of ASSBs exhibited superior stability with a 4 C rate and 5.72 mA cm^{-2} areal current density, which achieved up to 1400 cycles with 70% capacity retention. In contrast, when the LCO cathode was paired with the LInCl electrolyte or commercial liquid electrolyte and cycled up to 4.6 V, a substantial decrease in the capacity was observed, yielding only approximately 60 mA h g^{-1} after 200 cycles (Figure S16). Notably, our SSE exhibited a substantially high voltage limit, higher current density endurance, and excellent cycle life, holding great promises for the future application of energy-dense ASSBs.

Structural Stability and Interfacial Compatibility under 4.6 V. To gain a comprehensive understanding of the electrochemical reaction mechanism of LInTaCl in ASSBs, we conducted morphology analysis of the solid electrolyte materials and the cathode during cycling. As depicted in Figure 5a, LCO particles were surrounded by halide electrolyte particles and VGCF in the pristine cathode active materials. However, in the case of LInCl cathode active materials, we observed the formation of nanosized grains and structural damage on the surface of the LCO structure after 100 cycles (Figure 5b,c and the corresponding diameter distribution in Figure S19). In comparison, the LInTaCl cathode active materials maintain structural integrity and exhibit a similar morphology to the pristine samples (Figure 5d−f). Furthermore, we employed STEM to investigate the surface and bulk structures of cycled LCO electrodes. Figure S20a reveals that the $Fd\bar{3}m$ phase, characterized by a *d*-spacing of 4.4 Å, is present in the cycled LCO of the LiInCl ASSB.[51,52] This phase indicates an irreversible transition to a Co_3O_4 phase in the LCO. Additionally, we identified an amorphous nanolayer on the surface of the cycled LCO, further demonstrating that decomposition of the LCO particles has occurred. Conversely, this is shown in Figure S20b; the cycled LCO of LInTaCl ASSBs retains its original layered $R\bar{3}m$ structure with lattice spacings of 4.7 and 2.4 Å for the (003) and (100) planes, respectively, suggesting that it maintains structural stability under a voltage of 4.6 V. The LCO cathode materials suffer from irreversible oxidation destruction under high voltage during long-term cycling for the LCO//LInCl//LPSCl//Li−In ASSB,[53] leading to the accumulation of the decomposition products and hindrance in ionic and electronic transport with capacity fading as schematically illustrated in Figure 5g. The highly stable LInTaCl SSE plays a crucial role in preserving the oxygen redox activity of the ASSB, thereby enabling high voltage stability for a long cycling performance (Figure 5h).

To investigate the interfacial compatibility between LCO and LInTaCl (LInCl), we employed XPS to monitor the interfacial evolution. In the pristine LInCl (Figure S21), distinct peaks at 446.1 and 453 eV corresponding to ln $3d_{3/2}$ and $3d_{5/2}$, respectively, were observed, which can be attributed to Li_3InCl_6 as mentioned in previous studies.[39] After 100 cycles, two additional signals at 440.5 and 449 eV in the corresponding oxygen-containing In_2O_3 were observed alongside the original Li_3InCl_6 peak, indicating electrochemical side reactions between LInCl and LCO under high-voltage conditions.[54] For the cycled LCO in the LInCl ASSB, additional peaks at 781.3 and 801.3 eV characteristic of Co^{2+} indicate an irreversible transition to a Co_3O_4 phase (Figure S22a).[55] In contrast, as demonstrated in Figure 5i−k, no significant changes were observed in the In, Ta, and Cl chemistry of the LInTaCl SSE nor were characteristic Co^{2+} peaks of the LCO cathode detected in the XPS spectra after electrochemical cycling. The superior performance of the LInTaCl ASSB under high-voltage conditions originates from the enhancement of both chemical and structural stability by pentavalent tantalum (Ta^{5+}). By forming robust, stable bonds within the crystal lattice, Ta^{5+} fosters a denser, more robust structure (detailed in Table S6[39]), broadening the electrolyte's electrochemical window, which in turn enhances resistance to degradation and preserves structural integrity under high-voltage conditions.[50,56] To assess the stability of the electrode−electrolyte interphases during long-term cycling, we performed AC impedance measurements (Figure S23). In contrast to the LInCl ASSB, where impedance consistently rose throughout the cycling duration due to detrimental oxidation destruction, the ASSB with the LInTaCl SSE exhibited a stabilized impedance at approximately 33 Ω over the initial 100 cycles, enabling excellent cycling stability.

CONCLUSIONS

In summary, we reported a series of high-valent lithium chloride compounds with high ionic conductivity. The $Li_{2.6}In_{0.8}Ta_{0.2}Cl_6$ exhibited superionic conductivity of up to 4.47 mS cm^{-1} at 30 °C, a low activation energy barrier, and an expanded onset of electrochemical oxidation. AIMD simulation demonstrated the intrinsic high ion conductivity of the LInTaCl system. By analyzing the probability density of Li^+, the increase of cation vacancies in the doped LInCl lattice enhanced the percolation of lithium ions. The comprehensive characterization techniques have confirmed the presence of a stable interface between the cathode active materials and SSEs, thereby validating the high oxidation stability and chemical compatibility of LInTaCl with oxide cathode materials. Thus, ASSBs exhibited exceptional cycling stability, maintaining 70% capacity retention even at high current densities and high rates, specifically at a 4 C rate with an active material loading of 7.52 mg cm^{-2}, for over 1450 cycles. Significantly, future advancements are expected to prioritize these concepts into high-voltage ASSBs, aiming to meet the increasing energy density demand for next-generation 5 V batteries.

MATERIALS AND METHODS

Preparation of High-Valent Chloride Solid Electrolytes. Solid chloride electrolytes were prepared using a meticulous procedure under an inert argon atmosphere, ensuring minimal exposure to moisture and oxygen (H_2O, O_2 < 0.01 ppm). High-purity raw materials, including LiCl (Macklin, 99.9% trace metal basis), $InCl_3$ (Aladdin, 99.9%), $ZrCl_4$ (Macklin, 99.9%), $NbCl_5$ (Macklin, 99.9%), $TaCl_5$ (Macklin, 99.9%), and WCl_6 (Macklin, 99.9%), were procured and utilized as precursors. These precursors were accurately mixed in stoichiometric ratios. The resulting mixture, weighing approximately 1.5 g, was then placed in a zirconia ball-milling cup along with 15 zirconia balls, each with a diameter of 10

https://doi.org/10.1021/acsnano.4c02678
ACS Nano 2024, 18, 18368−18378

mm. To ensure thorough mixing of the precursors, a low-speed ball-milling process at 100 rpm was carried out for 1 h. Subsequently, a high-speed ball-milling process at 750 rpm was performed from 15 to 30 h. The ball-milled product was then transferred to a carbon crucible and sealed in a quartz tube under vacuum conditions. The annealing process was conducted at a heating rate of 5 °C per minute, maintaining a temperature of 260 °C for 5 h. Following natural cooling to RT, the SSE powders were transferred to a glovebox environment and manually ground into fine powders for subsequent use in further experiments (the SEM image and corresponding diameter distribution of the synthesized SSE are shown in Figure S7).

Characterization Methods. Powder XRD (PXRD) measurements were conducted using a Rigaku SmartLab instrument, scanning the range from 10° to 80° with Cu Kα radiation (45 kV, 200 mA). The samples were securely packed with a Kapton film during PXRD analysis to prevent air exposure and ensure accurate measurements. Synchrotron XRD (SXRD) measurements were performed at the PD Beamline, Australian Synchrotron, ANSTO. A Mythen-II detector was utilized, and the wavelength of the X-rays was set to 0.5921 Å with an energy of 21 keV. Rietveld refinements of the SXRD data were conducted using GSAS-II software. The crystal structure obtained from the refinements was visualized and analyzed by using VESTA software. High-angle annular dark-field scanning TEM images and EDS maps were acquired by using an aberration-corrected scanning transmission electron microscope (FEI Tian Themis) operating at 300 kV. This advanced microscope allowed for a detailed examination of the morphologies of chloride electrolytes and cathode active materials during the electrochemical processes. The FESEM technique, equipped with a HITACHI SU8010 instrument, was employed to investigate the morphologies of the chloride electrolytes and cathode active materials. This analysis provided valuable insights into the surface and structural characteristics of the materials during electrochemical processes. XPS measurements were performed using a Ulvac-PHI PHI 5000 VersaProbe instrument coupled with a vacuum transfer system. The XPS analysis was conducted with a current of 25 mA and a voltage of 15 kV.

Calculation Methods. All density functional theory calculations in this work were performed using the Vienna ab initio simulation package within the projector augmented-wave approach.[57,58] The Perdew−Burke−Ernzerhof (PBEsol) generalized gradient approximation functional was used, designed to improve upon PBE for equilibrium properties of bulk solids.[59,60] The cutoff energy was set to 520 eV. The energy convergence criterion was adjusted to 1×10^{-4} eV. A K-point resolved value of 0.04 2π/Å was used for structural optimization and a gamma-only k-point grid was used in AIMD simulations. AIMD simulations adopted the NVT ensemble with a time step of 1 fs.[61] The Li^+ probability density was calculated as the time fraction of Li^+ at each spatial location during the AIMD simulations within Python Materials Genomics (pymatgen) code.[62,63]

The diffusion coefficient was calculated by mean square displacement over time intervals according to the Einstein relation

$$D = \frac{1}{2Nd\Delta t} \sum_{i=1}^{N} \langle |\mathbf{r}_i(t + \Delta t) - \mathbf{r}_i(t)|^2 \rangle_t$$

where N is the number of mobile ions, d is the dimension of the system, and $\mathbf{r}_i(t)$ is the trajectory of the ion at time t. The ionic conductivity was derived from the Nernst−Einstein relation

$$\sigma = \frac{Nq^2}{Vk_BT} D$$

where q is the ionic charge, V is the volume of the structure, and k_B is the Boltzmann constant.

The activation energy E_a was obtained from the Arrhenius relation

$$D = D_0 \exp\left(-\frac{E_a}{k_BT}\right)$$

The conductivity at RT was obtained by extrapolating the Arrhenius relation to 300 K. The statistical variance of the diffusivity and ionic conductivity were quantified with the method proposed by He et al.[64]

Electrochemical Measurements. Ionic conductivity measurements were performed by using EIS. Approximately 120 mg of the halide electrolyte powder was pressed into a 10 mm diameter pellet between two stainless steel rods using a hydraulic press at 4 tons of pressure for 1 min. The EIS experiments were conducted at 30 °C, applying a constant voltage of 10 mV over a frequency range of 7 MHz to 1 Hz. A VMP3 potentiostat/galvanostat from BioLogic was employed for these measurements. To determine the activation energies, temperature-dependent EIS measurements were conducted in the temperature range of 30−70 °C, following the Arrhenius formula. LSV measurements were performed by using an indium anode and a composite cathode consisting of LInTaCl and VGCF in a weight ratio of 70:30. The LSV experiments were carried out using a SOLARTRON electrochemical workstation. The scan range was set from OCP to 6 V versus Li/Li^+. To prepare the working electrode, 80 mg of LInTaCl powder was cold-pressed into a pellet under a pressure of 3 tons. Subsequently, a mixture of 10 mg of SSEs and VGCF was uniformly placed on one side of the LInTaCl pellet and compressed again under the same pressure. An In foil (obtained from Dongxia Co., Ltd, Shenzhen) was attached to the other side of the pellet, serving as both the counter and reference electrode. To ensure compatibility between LInTaCl and the metallic anode, a thinner layer of a sulfide SSE (approximately 30 mg of LPSCl, purchased from Ganfeng Lithium Industry, China; 5.5 mS cm^{-1} at 30 °C) was inserted as a protective interface.

ASSB Construction. ASSBs were constructed using chloride SSEs in combination with $LiCoO_2$ (Youyan Materials Co., Ltd.) and $LiNi_{0.8}Co_{0.1}Mn_{0.1}O_2$ (NCM811, Rongbai Co., Ltd.) cathode active materials and an In/InLi anode. Before use, all cathode active materials were dried at 200 °C for 12 h in an Ar-filled glovebox. The assembly process involved several steps. First, approximately 40 mg of LPSCl powder was placed into a PEEK cylinder and pressed at 3 tons for 1 min to form a pellet with a diameter of 10 mm. Then, approximately 60 mg of LInTaCl was spread over one side of the LPSCl pellet, and the assembly was pressed at 2 tons for another 1 min. The composite cathode mixtures were prepared by mixing LCO or NCM811, LInTaCl, and VGCF in a weight ratio of 7:2.5:0.5. On the LInTaCl side of the SSE pellet, 6.5−8.5 mg of the composite cathode mixture was spread and pressed at 3 tons for 2 min. On the other side of the pellet, a thin indium foil (9 mm diameter, 99.999%, 0.1 mm thickness) was attached, and a 6 mm diameter Li foil was placed over the indium foil. The assembled cell was then placed into a custom-made stainless steel casing with a constant applied pressure of about 125 MPa during cycling. All the cells were tested at 30 °C. The measurements of the ASSBs were conducted using the NEWARE Battery Test System (CT-4008Tn, Shenzhen, China).

Assembly of LCO Liquid Cells. To fabricate the electrodes, LCO powder was mixed with Super P carbon (Youyan Materials) and poly(vinylidene fluoride) (Youyan Materials, average $M_w \sim 1{,}000{,}000$ GPC) in a weight ratio of 8:1:1 (active material/carbon/binder). The resulting powdered mixture was then suspended in N-methyl-2-pyrrolidinone (Aladdin, 99.5%) to form a viscous slurry. This slurry was cast onto Al foil, with a typical loading of approximately 3.0 mg cm^{-2}, and subsequently dried in a vacuum oven at 120 °C overnight. Electrochemical studies were conducted using 2025 coin-type half-cells, consisting of a Li-metal anode, Celgard 3501 separator, and a liquid electrolyte (Canrd, 1 M $LiPF_6$ in ethylene carbonate/ethylmethyl carbonate/diethyl carbonate at a ratio of 1:1:1).

ASSOCIATED CONTENT

Supporting Information

The Supporting Information is available free of charge at https://pubs.acs.org/doi/10.1021/acsnano.4c02678.

Characterizations of high-valent doped SSEs such as XRD, EIS, SEM, EDS, and Rietveld refinement profiles; AIMD simulation details; electrochemical tests of LSV

https://doi.org/10.1021/acsnano.4c02678
ACS Nano 2024, 18, 18368−18378

profiles, CV results, charge/discharge profiles, and AC impedance spectra; and STEM and XPS spectra of the electrode materials after charge/discharge (PDF)

Crystallographic data of $Li_{2.6}In_{0.8}Ta_{0.2}Cl_6$ (CIF)

AUTHOR INFORMATION

Corresponding Authors

Xihan Chen − *Department of Mechanical and Energy Engineering, Southern University of Science and Technology, Shenzhen 518055, China;* orcid.org/0000-0001-7907-2549; Email: chenxh@sustech.edu.cn

Haw Jiunn Woo − *Centre for Ionics University of Malaya, Department of Physics, Faculty of Science, University of Malaya, Kuala Lumpur 50603, Malaysia;* orcid.org/0000-0002-1126-0153; Email: woohj@um.edu.my

Yizhou Zhu − *Research Center for Industries of the Future and School of Engineering, Westlake University, Hangzhou, Zhejiang 310030, China;* orcid.org/0000-0002-5819-7657; Email: zhuyizhou@westlake.edu.cn

Jiayu Wan − *Future Battery Research Center, Global Institute of Future Technology, Shanghai Jiaotong University, Shanghai 200240, China;* orcid.org/0000-0003-4603-3265; Email: wanjy@sjtu.edu.cn

Authors

Yu Ye − *Department of Mechanical and Energy Engineering, Southern University of Science and Technology, Shenzhen 518055, China; Future Battery Research Center, Global Institute of Future Technology, Shanghai Jiaotong University, Shanghai 200240, China; Centre for Ionics University of Malaya, Department of Physics, Faculty of Science, University of Malaya, Kuala Lumpur 50603, Malaysia*

Jiazhong Geng − *Research Center for Industries of the Future and School of Engineering, Westlake University, Hangzhou, Zhejiang 310030, China*

Daxian Zuo − *Department of Mechanical and Energy Engineering, Southern University of Science and Technology, Shenzhen 518055, China*

Kangdi Niu − *Department of Physics, Southern University of Science and Technology, Shenzhen 518055, China*

Diancheng Chen − *Department of Physics, Southern University of Science and Technology, Shenzhen 518055, China*

Junhao Lin − *Department of Physics, Southern University of Science and Technology, Shenzhen 518055, China;* orcid.org/0000-0002-2195-2823

Complete contact information is available at: https://pubs.acs.org/10.1021/acsnano.4c02678

Author Contributions

[#]Y.Y., J.G., and D.Z. contributed equally to this work.

Notes

The authors declare no competing financial interest.

ACKNOWLEDGMENTS

The authors gratefully acknowledge the support from the National Natural Science Foundation of China (52272215), the Research Center for Industries of the Future (RCIF), and the High-Performance Computing Center (HPC) at Westlake University.

REFERENCES

(1) Xiao, J.; Shi, F.; Glossmann, T.; Burnett, C.; Liu, Z. From Laboratory Innovations to Materials Manufacturing for Lithium-Based Batteries. *Nat. Energy* **2023**, *8*, 329−339.

(2) Xu, K. Electrolytes and Interphases in Li-ion Batteries and Beyond. *Chem. Rev.* **2014**, *114*, 11503−11618.

(3) Huang, Y.; Li, J. Key Challenges for Grid-scale Lithium-Ion Battery Energy Storage. *Adv. Energy Mater.* **2022**, *12*, 2202197.

(4) Manthiram, A.; Yu, X.; Wang, S. Lithium Battery Chemistries Enabled by Solid-State Electrolytes. *Nat. Rev. Mater.* **2017**, *2*, 16103.

(5) Famprikis, T.; Canepa, P.; Dawson, J. A.; Islam, M. S.; Masquelier, C. Fundamentals of Inorganic Solid-State Electrolytes for Batteries. *Nat. Mater.* **2019**, *18*, 1278−1291.

(6) Xiao, C. F.; Kim, J. H.; Cho, S. H.; Park, Y. C.; Kim, M. J.; Chung, K. B.; Yoon, S. G.; Jung, J. W.; Kim, I. D.; Kim, H. S. Ensemble Design of Electrode-Electrolyte Interfaces: Toward High-Performance Thin-Film All-Solid-State Li-Metal Batteries. *ACS Nano* **2021**, *15*, 4561−4575.

(7) Zhao, Q.; Stalin, S.; Zhao, C.-Z.; Archer, L. A. Designing Solid-State Electrolytes for Safe, Energy-Dense Batteries. *Nat. Rev. Mater.* **2020**, *5*, 229−252.

(8) Meng, Y. S.; Srinivasan, V.; Xu, K. Designing Better Electrolytes. *Science* **2022**, *378*, No. eabq3750.

(9) Janek, J.; Zeier, W. G. Challenges in Speeding Up Solid-State Battery Development. *Nat. Energy* **2023**, *8*, 230−240.

(10) Kim, K. J.; Balaish, M.; Wadaguchi, M.; Kong, L.; Rupp, J. L. M. Solid-State Li-Metal Batteries: Challenges and Horizons of Oxide and Sulfide Solid Electrolytes and Their Interfaces. *Adv. Energy Mater.* **2020**, *11*, 2002689.

(11) Feng, Y.; Yang, L.; Yan, Z.; Zuo, D.; Zhu, Z.; Zeng, L.; Zhu, Y.; Wan, J. Discovery of High Entropy Garnet Solid-State Electrolytes via Ultrafast Synthesis. *Energy Storage Mater.* **2023**, *63*, 103053.

(12) Zuo, D.; Yang, L.; Zou, Z.; Li, S.; Feng, Y.; Harris, S. J.; Shi, S.; Wan, J. Ultrafast Synthesis of NASICON Solid Electrolytes for Sodium-Metal Batteries. *Adv. Energy Mater.* **2023**, *13*, 103053.

(13) Alexander, G. V.; Shi, C.; O'Neill, J.; Wachsman, E. D. Extreme Lithium-Metal Cycling Enabled by a Mixed Ion- and Electron-Conducting Garnet Three-Dimensional Architecture. *Nat. Mater.* **2023**, *22*, 1136−1143.

(14) Zhu, Y.; Gonzalez-Rosillo, J. C.; Balaish, M.; Hood, Z. D.; Kim, K. J.; Rupp, J. L. M. Lithium-Film Ceramics for Solid-State Lithionic Devices. *Nat. Rev. Mater.* **2020**, *6*, 313−331.

(15) Kato, Y.; Hori, S.; Saito, T.; Suzuki, K.; Hirayama, M.; Mitsui, A.; Yonemura, M.; Iba, H.; Kanno, R. High-Power All-Solid-State Batteries Using Sulfide Superionic Conductors. *Nat. Energy* **2016**, *1*, 16030.

(16) Lee, Y.-G.; Fujiki, S.; Jung, C.; Suzuki, N.; Yashiro, N.; Omoda, R.; Ko, D.-S.; Shiratsuchi, T.; Sugimoto, T.; Ryu, S.; Ku, J. H.; Watanabe, T.; Park, Y.; Aihara, Y.; Im, D.; Han, I. T. High-Energy Long-Cycling All-Solid-State Lithium Metal Batteries Enabled by Silver-Carbon Composite Anodes. *Nat. Energy* **2020**, *5*, 299−308.

(17) Li, Y.; Song, S.; Kim, H.; Nomoto, K.; Kim, H.; Sun, X.; Hori, S.; Suzuki, K.; Matsui, N.; Hirayama, M.; Mizoguchi, T.; Saito, T.; Kamiyama, T.; Kanno, R. A Lithium Superionic Conductor for Millimeter-Thick Battery Electrode. *Science* **2023**, *381*, 50−53.

(18) Ma, Y.; Wan, J.; Xu, X.; Sendek, A. D.; Holmes, S. E.; Ransom, B.; Jiang, Z.; Zhang, P.; Xiao, X.; Zhang, W.; Xu, R.; Liu, F.; Ye, Y.; Kaeli, E.; Reed, E. J.; Chueh, W. C.; Cui, Y. Experimental Discovery of a Fast and Stable Lithium Thioborate Solid Electrolyte, $Li_{6+2x}[B_{10}S_{18}]S_x$ ($x \approx 1$). *ACS Energy Lett.* **2023**, *8*, 2762−2771.

(19) Liang, Z.; Xiang, Y.; Wang, K.; Zhu, J.; Jin, Y.; Wang, H.; Zheng, B.; Chen, Z.; Tao, M.; Liu, X.; Wu, Y.; Fu, R.; Wang, C.; Winter, M.; Yang, Y. Understanding the Failure Process of Sulfide-Based All-Solid-State Lithium Batteries via Operando Nuclear Magnetic Resonance Spectroscopy. *Nat. Commun.* **2023**, *14*, 259.

(20) Liu, S.; Zhou, L.; Han, J.; Wen, K.; Guan, S.; Xue, C.; Zhang, Z.; Xu, B.; Lin, Y.; Shen, Y.; Li, L.; Nan, C. W. Super Long-Cycling All-Solid-State Battery with Thin Li_6PS_5Cl-Based Electrolyte. *Adv. Energy Mater.* **2022**, *12*, 2200660.

(21) Li, X.; Liang, J.; Yang, X.; Adair, K. R.; Wang, C.; Zhao, F.; Sun, X. Progress and Perspectives on Halide Lithium Conductors for All-Solid-State Lithium Batteries. *Energy Environ. Sci.* **2020**, *13*, 1429−1461.
(22) Asano, T.; Sakai, A.; Ouchi, S.; Sakaida, M.; Miyazaki, A.; Hasegawa, S. Solid Halide Electrolytes with High Lithium-Ion Conductivity for Application in 4 V Class Bulk-Type All-Solid-State Batteries. *Adv. Mater.* **2018**, *30*, No. e1803075.
(23) Li, X.; Liang, J.; Chen, N.; Luo, J.; Adair, K. R.; Wang, C.; Banis, M. N.; Sham, T. K.; Zhang, L.; Zhao, S.; Lu, S.; Huang, H.; Li, R.; Sun, X. Water-Mediated Synthesis of a Superionic Halide Solid Electrolyte. *Angew. Chem., Int. Ed.* **2019**, *58*, 16427−16432.
(24) Liang, J.; Li, X.; Wang, S.; Adair, K. R.; Li, W.; Zhao, Y.; Wang, C.; Hu, Y.; Zhang, L.; Zhao, S.; Lu, S.; Huang, H.; Li, R.; Mo, Y.; Sun, X. Site-Occupation-Tuned Superionic Li_xScCl_{3+X} Halide Solid Electrolytes for All-Solid-State Batteries. *J. Am. Chem. Soc.* **2020**, *142*, 7012−7022.
(25) Zhou, L.; Zuo, T.-T.; Kwok, C. Y.; Kim, S. Y.; Assoud, A.; Zhang, Q.; Janek, J.; Nazar, L. F. High Areal Capacity, Long Cycle Life 4 V Ceramic All-Solid-State Li-Ion Batteries Enabled by Chloride Solid Electrolytes. *Nat. Energy* **2022**, *7*, 83−93.
(26) Wang, K.; Ren, Q.; Gu, Z.; Duan, C.; Wang, J.; Zhu, F.; Fu, Y.; Hao, J.; Zhu, J.; He, L.; Wang, C. W.; Lu, Y.; Ma, J.; Ma, C. A Cost-Effective and Humidity-Tolerant Chloride Solid Electrolyte for Lithium Batteries. *Nat. Commun.* **2021**, *12*, 4410.
(27) Ishiguro, Y.; Ueno, K.; Nishimura, S.; Iida, G.; Igarashib, Y. $Tacl_5$-Glassified Ultrafast Lithium Ion-Conductive Halide Electrolytes for High-Performance All-Solid-State Lithium Batteries. *Chem. Lett.* **2023**, *52*, 237−241.
(28) Hu, L.; Wang, J.; Wang, K.; Gu, Z.; Xi, Z.; Li, H.; Chen, F.; Wang, Y.; Li, Z.; Ma, C. A Cost-Effective, Ionically Conductive and Compressible Oxychloride Solid-State Electrolyte for Stable All-Solid-State Lithium-Based Batteries. *Nat. Commun.* **2023**, *14*, 3807.
(29) Tanaka, Y.; Ueno, K.; Mizuno, K.; Takeuchi, K.; Asano, T.; Sakai, A. New Oxyhalide Solid Electrolytes with High Lithium Ionic Conductivity > 10 mS cm^{-1} for All-Solid-State Batteries. *Angew. Chem., Int. Ed.* **2023**, *62*, No. e202217581.
(30) Kwak, H.; Wang, S.; Park, J.; Liu, Y.; Kim, K. T.; Choi, Y.; Mo, Y.; Jung, Y. S. Emerging Halide Superionic Conductors for All-Solid-State Batteries: Design, Synthesis, and Practical Applications. *ACS Energy Lett.* **2022**, *7*, 1776−1805.
(31) Helm, B.; Schlem, R.; Wankmiller, B.; Banik, A.; Gautam, A.; Ruhl, J.; Li, C.; Hansen, M. R.; Zeier, W. G. Exploring Aliovalent Substitutions in the Lithium Halide Superionic Conductor $Li_{3-x}In_{1-x}Zr_xCl_6$ ($0 \leq x \leq 0.5$). *Chem. Mater.* **2021**, *33*, 4773−4782.
(32) Park, K.-H.; Kaup, K.; Assoud, A.; Zhang, Q.; Wu, X.; Nazar, L. F. High-Voltage Superionic Halide Solid Electrolytes for All-Solid-State Li-Ion Batteries. *ACS Energy Lett.* **2020**, *5*, 533−539.
(33) Yin, Y. C.; Yang, J. T.; Luo, J. D.; Lu, G. X.; Huang, Z.; Wang, J. P.; Li, P.; Li, F.; Wu, Y. C.; Tian, T.; Meng, Y. F.; Mo, H. S.; Song, Y. H.; Yang, J. N.; Feng, L. Z.; Ma, T.; Wen, W.; Gong, K.; Wang, L. J.; Ju, H. X.; et al. A $LaCl_3$-Based Lithium Superionic Conductor Compatible with Lithium Metal. *Nature* **2023**, *616*, 77−83.
(34) Wang, S.; Bai, Q.; Nolan, A. M.; Liu, Y.; Gong, S.; Sun, Q.; Mo, Y. Lithium Chlorides and Bromides as Promising Solid-State Chemistries for Fast Ion Conductors with Good Electrochemical Stability. *Angew. Chem., Int. Ed.* **2019**, *58*, 8039−8043.
(35) Chen, Y.; Rangasamy, E.; Liang, C. Origin of High Li^+ Conduction in Doped $Li_7La_3Zr_2O_{12}$ Garnets. *Chem. Mater.* **2015**, *27* (16), 5491−5494.
(36) Raju, M. M.; Altayran, F.; Johnson, M.; Wang, D.; Zhang, Q. Crystal Structure and Preparation of $Li_7La_3Zr_2O_{12}$ (LLZO) Solid-State Electrolyte and Doping Impacts on the Conductivity: An Overview. *Electro. Chem.* **2021**, *2*, 390−414.
(37) Liu, Y.; Wang, S.; Nolan, A. M.; Ling, C.; Mo, Y. Tailoring the Cation Lattice for Chloride Lithium-Ion Conductors. *Adv. Energy Mater.* **2020**, *10*, 2002356.
(38) Zhang, S.; Zhao, F.; Wang, S.; Liang, J.; Wang, J.; Wang, C.; Zhang, H.; Adair, K.; Li, W.; Li, M.; Duan, H.; Zhao, Y.; Yu, R.; Li, R.; Huang, H.; Zhang, L.; Zhao, S.; Lu, S.; Sham, T. K.; Mo, Y.; Sun, X. Advanced High-Voltage All-Solid-State Li-Ion Batteries Enabled by a Dual-Halogen Solid Electrolyte. *Adv. Energy Mater.* **2021**, *11*, 2100836.
(39) Li, X.; Liang, J.; Luo, J.; Norouzi Banis, M.; Wang, C.; Li, W.; Deng, S.; Yu, C.; Zhao, F.; Hu, Y.; Sham, T.-K.; Zhang, L.; Zhao, S.; Lu, S.; Huang, H.; Li, R.; Adair, K. R.; Sun, X. Air-Stable Li_3InCl_6 Electrolyte with High Voltage Compatibility for All-Solid-State Batteries. *Energy Environ. Sci.* **2019**, *12*, 2665−2671.
(40) Cao, G.; Liang, J.; Guo, Z.; Yang, K.; Wang, G.; Wang, H.; Wan, X.; Li, Z.; Bai, Y.; Zhang, Y.; Liu, J.; Feng, Y.; Zheng, Z.; Lu, C.; He, G.; Xiong, Z.; Liu, Z.; Chen, S.; Guo, Y.; Zeng, M.; Lin, J.; Fu, L. Liquid Metal for High-Entropy Alloy Nanoparticles Synthesis. *Nature* **2023**, *619*, 73−77.
(41) Kwak, H.; Han, D.; Lyoo, J.; Park, J.; Jung, S. H.; Han, Y.; Kwon, G.; Kim, H.; Hong, S. T.; Nam, K. W.; Jung, Y. S. New Cost-Effective Halide Solid Electrolytes for All-Solid-State Batteries: Mechanochemically Prepared Fe^{3+}-Substituted Li_2ZrCl_6. *Adv. Energy Mater.* **2021**, *11*, 2003190.
(42) Liang, J.; van der Maas, E.; Luo, J.; Li, X.; Chen, N.; Adair, K. R.; Li, W.; Li, J.; Hu, Y.; Liu, J.; Zhang, L.; Zhao, S.; Lu, S.; Wang, J.; Huang, H.; Zhao, W.; Parnell, S.; Smith, R. I.; Ganapathy, S.; Wagemaker, M.; Sun, X. A Series of Ternary Metal Chloride Superionic Conductors for High-Performance All-Solid-State Lithium Batteries. *Adv. Energy Mater.* **2022**, *12*, 2103921.
(43) Kim, S. Y.; Kaup, K.; Park, K.-H.; Assoud, A.; Zhou, L.; Liu, J.; Wu, X.; Nazar, L. F. Lithium Ytterbium-Based Halide Solid Electrolytes for High Voltage All-Solid-State Batteries. *ACS Mater. Lett.* **2021**, *3*, 930−938.
(44) Nolan, A. M.; Zhu, Y.; He, X.; Bai, Q.; Mo, Y. Computation-Accelerated Design of Materials and Interfaces for All-Solid-State Lithium-Ion Batteries. *Joule* **2018**, *2*, 2016−2046.
(45) Rosenbach, C.; Walther, F.; Ruhl, J.; Hartmann, M.; Hendriks, T. A.; Ohno, S.; Janek, J.; Zeier, W. G. Visualizing the Chemical Incompatibility of Halide and Sulfide-Based Electrolytes in Solid-State Batteries. *Adv. Energy Mater.* **2022**, *13*, 2203673.
(46) Wang, C.; Liang, J.; Luo, J.; Liu, J.; Li, X.; Zhao, F.; Li, R.; Huang, H.; Zhao, S.; Zhang, L.; Wang, J.; Sun, X. A Universal Wet-Chemistry Synthesis of Solid-State Halide Electrolytes for All-Solid-State Lithium-Metal Batteries. *Sci. Adv.* **2021**, *7*, No. eabh1896.
(47) Kochetkov, I.; Zuo, T.; Ruess, R.; Singh, B.; Zhou, L.; Kaup, K.; Janek, J.; Nazar, L. Different Interfacial Reactivity of Lithium Metal Chloride Electrolytes with High Voltage Cathodes Determines Solid-State Battery Performance. *Energy Environ. Sci.* **2022**, *15*, 3933−3944.
(48) Nikodimos, Y.; Su, W. N.; Hwang, B. J. Halide Solid-State Electrolytes: Stability and Application for High Voltage All-Solid-State Li Batteries. *Adv. Energy Mater.* **2022**, *13*, 2202854.
(49) Wang, C.; Wang, S.; Liu, X.; Wu, Y.; Yu, R.; Duan, H.; Kim, J. T.; Huang, H.; Wang, J.; Mo, Y.; Sun, X. New Insights into Aliovalent Substituted Halide Solid Electrolytes for Cobalt-Free All-Solid-State Batteries. *Energy Environ. Sci.* **2023**, *16*, 5136−5143.
(50) Xu, G.; Luo, L.; Liang, J.; Zhao, S.; Yang, R.; Wang, C.; Yu, T.; Wang, L.; Xiao, W.; Wang, J.; Yu, J.; Sun, X. Origin of High Electrochemical Stability of Multi-Metal Chloride Solid Electrolytes for High Energy All-Solid-State Lithium-Ion Batteries. *Nano Energy* **2022**, *92*, 106674.
(51) Lu, G.; Geng, F.; Guo, N.; Yao, S.; Shen, M.; Hu, B. Probing the Degradation of $LiCoO_2$ in Batteries Subjected to High-Voltage Cycling with ^{17}O Solid-State NMR Spectroscopy. *Chem. Commun.* **2023**, *59*, 7959−7962.
(52) Yang, C.; Liao, X.; Zhou, X.; Sun, C.; Qu, R.; Han, J.; Zhao, Y.; Wang, L.; You, Y.; Lu, J. Phosphate-Rich Interface for a Highly Stable and Safe 4.6 V $LiCoO_2$ Cathode. *Adv. Mater.* **2023**, *35*, 2210966.
(53) Fan, T.; Kai, W.; Harika, V. K.; Liu, C.; Nimkar, A.; Leifer, N.; Maiti, S.; Grinblat, J.; Tsubery, M. N.; Liu, X.; Wang, M.; Xu, L.; Lu, Y.; Min, Y.; Shpigel, N.; Aurbach, D. Operating Highly Stable $LiCoO_2$ Cathodes up to 4.6 V by Using an Effective Integration of Surface Engineering and Electrolyte Solutions Selection. *Adv. Funct. Mater.* **2022**, *32*, 2204972.

https://doi.org/10.1021/acsnano.4c02678
ACS Nano 2024, 18, 18368−18378

(54) Riegger, L. M.; Schlem, R.; Sann, J.; Zeier, W. G.; Janek, J. Lithium-Metal Anode Instability of the Superionic Halide Solid Electrolytes and the Implications for Solid-State Batteries. *Angew. Chem., Int. Ed.* **2021**, *60*, 6718−6723.
(55) Guan, S.; Li, X.; Zhao, Y.; Han, G.; Lou, S.; Zhu, Y. Single-Atom Tailored Transition Metal Oxide Enhances D-P Hybridization in Catalytic Conversion for Lithium-Oxygen Batteries. *Chem. Eng. J.* **2024**, *488*, 151064.
(56) Park, G. T.; Namkoong, B.; Kim, S. B.; Liu, J.; Yoon, C. S.; Sun, Y. K. Introducing High-Valence Elements into Cobalt-Free Layered Cathodes for Practical Lithium-Ion Batteries. *Nat. Energy* **2022**, *7*, 946−954.
(57) Kresse, G.; Furthmüller, J. Efficient Iterative Schemes for Ab Initio Total-Energy Calculations Using a Plane-Wave Basis Set. *Phys. Rev. B: Condens. Matter Mater. Phys.* **1996**, *54*, 11169−11186.
(58) Blochl, P. E. Projector Augmented-Wave Method. *Phys. Rev. B: Condens. Matter Mater. Phys.* **1994**, *50*, 17953−17979.
(59) Perdew, J. P.; Ruzsinszky, A.; Csonka, G. I.; Vydrov, O. A.; Scuseria, G. E.; Constantin, L. A.; Zhou, X.; Burke, K. Restoring the Density-Gradient Expansion for Exchange in Solids and Surfaces. *Phys. Rev. Lett.* **2008**, *100*, 136406.
(60) Constantin, L. A.; Perdew, J. P.; Pitarke, J. M. Exchange-Correlation Hole of a Generalized Gradient Approximation for Solids and Surfaces. *Phys. Rev. B: Condens. Matter Mater. Phys.* **2009**, *79*, 075126.
(61) Nosé, S. Constant Temperature Molecular Dynamics Methods. *Prog. Theor. Phys. Suppl.* **1991**, *103*, 1−46.
(62) Zhu, Z.; Chu, I.-H.; Deng, Z.; Ong, S. P. Role of Na^+ Interstitials and Dopants in Enhancing the Na^+ Conductivity of the Cubic Na_3PS_4 Superionic Conductor. *Chem. Mater.* **2015**, *27*, 8318−8325.
(63) Ong, S. P.; Richards, W. D.; Jain, A.; Hautier, G.; Kocher, M.; Cholia, S.; Gunter, D.; Chevrier, V. L.; Persson, K. A.; Ceder, G. Python Materials Genomics (Pymatgen): a Robust, Open-Source Python Library for Materials Analysis. *Comput. Mater. Sci.* **2013**, *68*, 314−319.
(64) He, X.; Zhu, Y.; Epstein, A.; Mo, Y. Statistical Variances of Diffusional Properties from Ab Initio Molecular Dynamics Simulations. *npj Comput. Mater.* **2018**, *4*, 18.

https://doi.org/10.1021/acsnano.4c02678
ACS Nano 2024, 18, 18368−18378